crystals

MDPI

*Article*

# Facile Low-Temperature Deposition of Seedless Nanocrystalline Diamond Films from $CH_4$/Ar Gas Mixtures

**Luis Medina-Zazueta [1], Frank Romo-García [2], Miguel Martínez-Gil [2], Rolando Flores-Ochoa [2], Mathías Martinez-Gil [2], Dainet Berman-Mendoza [3], Antonio Ramos-Carrazco [3], Gerardo Valenzuela-Hernández [3], Ch. J. Salas-Juárez [4], Carlos A. Pérez-Rábago [5] and Rafael García-Gutiérrez [3,*]**

[1] Departamento de Física, Universidad de Sonora, Hermosillo 83000, Sonora, Mexico; a219230174@unison.mx
[2] Departamento de Física Matemáticas e Ingeniería, Universidad de Sonora, Navojoa 85880, Sonora, Mexico; frank.romo@unison.mx (F.R.-G.); miguel.martinezgil@unison.mx (M.M.-G.); rolando.flores@unison.mx (R.F.-O.); mathias.martinez@unison.mx (M.M.-G.)
[3] Departamento de Investigación en Física, Universidad de Sonora, Hermosillo 83000, Sonora, Mexico; dainet.berman@unison.mx (D.B.-M.); antonio.ramos@unison.mx (A.R.-C.); gerardo.valenzuela@unison.mx (G.V.-H.)
[4] Área de Química, Departamento de Ciencias Básicas, Universidad Autónoma Metropolitana Azcapotzalco, Av. San Pablo No. 420, Col. Nueva el Rosario, Azcapotzalco, Ciudad de México 02128, Mexico; cjsj@azc.uam.mx
[5] Instituto de Energías Renovables, Universidad Nacional Autónoma de México Priv. Xochicalco, Temixco 62580, Morelos, Mexico; capr@ier.unam.mx
* Correspondence: rafael.gutierrez@unison.mx

## Abstract

Nanocrystalline diamond (NCD) films were synthesized by microwave plasma chemical vapor deposition (MPCVD) from a $CH_4$/Ar mixture on seedless p-type Si(111) substrates at 100–400 °C. Crystallinity was evaluated by X-ray diffraction (Cu Kα); bonding by Raman spectroscopy and X-ray photoelectron spectroscopy (XPS); morphology and thickness by scanning electron microscopy (SEM); defect states by thermoluminescence (TL). SEM shows continuous films with uniform thickness. XRD displays a broad (111) reflection near $2\theta = 44°$. Raman and XPS reveal temperature-dependent bonding: between 300 and 400 °C, the $sp^3$ fraction increases relative to $sp^2$. TL glow curves show peaks at 157 °C and 270 °C, indicating electron-trap centers. These results demonstrate hydrogen-free and seedless NCD growth at low substrate temperatures, supporting potential electronic and dosimetry applications requiring a low thermal load.

**Keywords:** nanocrystalline diamond (NCD); microwave plasma chemical vapor deposition (MPCVD); seedless growth; low-temperature deposition; hydrogen-free growth

Check for updates

Academic Editors: Abdellatif El-Habib and Abdessamad Aouni

Received: 26 November 2025
Revised: 18 December 2025
Accepted: 20 December 2025
Published: 24 December 2025

**Copyright:** © 2025 by the authors. Licensee MDPI, Basel, Switzerland. This article is an open access article distributed under the terms and conditions of the Creative Commons Attribution (CC BY) license.

## 1. Introduction

Diamond is recognized for a unique combination of properties. These include exceptional thermal conductivity and numerous distinctive features compared to other materials. Its excellent thermal conductivity, wear resistance, electrical insulation, chemical inertness, negative electronic affinity, and biocompatibility with the human body make diamond thin films suitable for use in the medical and technology industries [1–5]. Tuning the electrical characteristics of nanocrystalline diamond (NCD) through doping (e.g., nitrogen or boron) further motivates its use in next-generation electronic devices [6,7].

Several studies have been conducted on the obtention of NCD films using a variety of experimental methods, including hot-filament chemical vapor deposition (HFCVD), microwave plasma CVD, oxyacetylene laminar flame, and arc-discharge plasma-jet CVD [8–10]. Due to the advantages of producing an electrodeless discharge and high-density plasma, as well as the ability to synthesize high-quality diamond, microwave plasma chemical vapor deposition (MPCVD) has been widely used to produce NCD [11].

Recently, reports have established the importance of nucleation seeds or substrate preparation for the synthesis of high-quality NCD films via MPCVD [12–14]. However, Ali et al. (2012) [15] reports the production of seedless diamond films of comparable quality, leaving the contradictory position discussed to this day. They attributed this possibility to the modification of the diamond phase composition as a function of methane concentration ($CH_4$), showing that lower $CH_4$ levels favor the formation of non-diamond phases, while higher $CH_4$ levels promote diamond growth, underscoring the importance of gas composition in NCD film properties.

Furthermore, the experimental procedure for synthesizing nanostructured diamond thin films suggests the use of the well-known $CH_4/Ar/H_2$ gas mixture [16]. However, the possibility of growing such films using only a $CH_4$-Ar mixture, without molecular hydrogen, has been previously demonstrated [17]. McCauley et al. (1998) [18] proposed an alternative mechanism for the growth of diamond films originating from carbon dimers ($C_2$) in an Ar environment. Their methodology suggests a reduction in energy activation during growth with $CH_4/Ar$ compared to $CH_4/H_2$. It has been demonstrated that $Ar/CH_4$-enriched plasma generates a complex mixture of carbonaceous species, specifically $C_2$ carbon dimers and a variety of hydrocarbons, including $CH_3$, among others, implying the essential role of $C_2$ dimers in the nucleation and growth processes of nanostructured diamond thin films [19].

Additionally, the absence of hydrogen in the precursor gas mixture directly reduces the activation temperature in the NCD experimental procedure. According to Xiao et al. (2004) [20], the $CH_4/H_2$ gas mixture requires an activation energy of 23 kcal/mol, whereas the $CH_4/Ar$ mixture requires less than 8 kcal/mol. The reduction in the activation energy facilitates the synthesis of diamond film at lower temperatures, enhancing its compatibility for several applications. Based on the latter, the possibility of depositing nanocrystalline diamond films below 500 °C has been proposed [21,22].

Conventional $H_2$-containing MPCVD typically requires higher substrate temperatures and a separate nanodiamond seeding step, leading to particle-handling variability and complicating processing on temperature-sensitive substrates [16]. By contrast, $Ar/ CH_4$ plasmas enable seedless nucleation and low-temperature growth (100–400 °C) without molecular hydrogen [17,20–22]. Furthermore, Ar-assisted pathways and carbon-dimer chemistry have been proposed to lower the effective activation barriers relative to $CH_4/H_2$ [19,23]. Removing $H_2$ simplifies gas handling, and eliminating seeding reduces cleanroom cross-contamination risks and process variability [13,24]. These factors make hydrogen-free, seedless NCD a useful complementary route to conventional $H_2$-assisted growth, especially for low-thermal-budget integration in sensors, microelectronics, and optoelectronic platforms [25].

Here, we report seedless, hydrogen-free nanocrystalline diamond (NCD) films grown by MPCVD ($CH_4/Ar$) at low substrate temperatures on p-type Si (111). Phase formation is established by combining Raman spectroscopy with X-ray diffraction (Cu Kα), showing a reflection at 44.3° ($2\theta$) indexed to cubic diamond (111). XPS tracks the temperature-dependent evolution of $sp^2/sp^3$ bonding; SEM documents film continuity and thickness; thermoluminescence (TL) probes defect-related trap centers. By removing $H_2$ and seeding, we suppress hydrogen-assisted chemistry and the variability introduced by nanodiamond

particle polydispersity and potential particle contamination (cross-contamination) and assess the low-activation-energy regime characteristic of low-temperature $CH_4$/Ar plasmas. Further details on the growth approach and characterization are provided below.

## 2. Materials and Methods

A schematic of the home-built microwave plasma chemical vapor deposition (MPCVD) system used to synthesize nanocrystalline diamond (NCD) films is shown in Figure 1. The system employs a 2.45 GHz microwave source (maximum output of 1.2 kW) coupled to a 25 mm high-purity quartz tube, which serves as the microwave optical window. The reaction chamber is composed of a quartz tube of an inner diameter of 50 mm with stainless-steel flanges. Process gases ($CH_4$/Ar) are delivered by two Aalborg Instruments and Controls, Inc., Orangeburg, NY, USA; model GFC17A series mass-flow controllers.

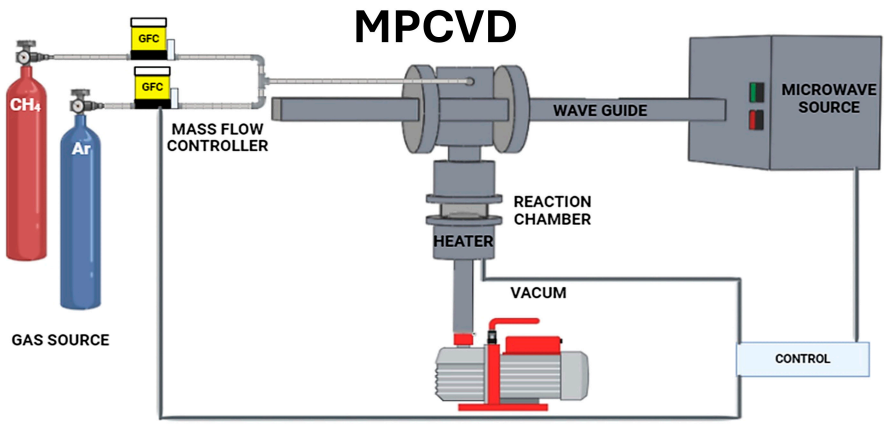


**Figure 1.** Schematic representation of the homemade MPCVD system used in this research to grow NCD films on silicon wafers. Note: Colors are used for illustrative purposes only; in this schematic, $CH_4$ is shown in red and Ar in blue for visual distinction, and green/red indicators denote ON/OFF.

A piece 2 cm long, 1 cm wide, and 2 mm thick was cleaved from a p-type Si (111) wafer and placed on a stainless-steel holder inside the MPCVD chamber (Figure 1). The holder was mounted on a 50 mm-diameter MHI GAX spiral heater (Micropyretics Heaters International, Cincinnati, OH, USA) to provide substrate heating. Before deposition, the chamber was evacuated to 6 Pa. NCD films were synthesized at substrate temperatures of 100, 200, 300, and 400 °C. During deposition, the process gas was a 2% methane ($CH_4$, 99.999%)/98% argon (Ar, 99.999%) mixture with a total flow of 110 sccm and a working pressure of 0.5 kPa. The microwave source (2.45 GHz) was set to 600 W to sustain plasma with a deposition time of 1 h. After growth, samples were cooled in Ar (80 sccm) to room temperature and then removed for subsequent analyses.

Raman spectra of the NCD films were acquired with a (alpha300, WITec Wissenschaftliche Instrumente und Technologie GmbH, Ulm, Germany) using a 532 nm laser excitation under identical optical conditions across samples. Grazing-incidence X-ray diffraction (GIXRD) was performed using a SmartLab diffractometer (Rigaku Corporation, Akishima, Tokyo, Japan) equipped with Cu K$\alpha$ radiation ($\lambda$ = 1.54 Å), scanning the range $2\theta$ = 40–80° with a counting time of 1 s per step and a step size of 0.02°.

XPS measurements were carried out on a PHI 5100 system (Physical Electronics, Inc., Chanhassen, MN, USA) with a Mg K$\alpha$ source (1253.6 eV) and a hemispherical analyzer operated at a 20 eV pass energy. Surface morphology and cross-sections were examined using a field-emission SEM (JSM-7800F, JEOL Ltd., Akishima, Tokyo, Japan) at an accelerating voltage of 5 kV. TL glow curves were recorded at a linear heating rate $\beta$ = 5 °C $s^{-1}$ from room temperature to 400 °C in $N_2$ using an automated TL/OSL reader (Risø

TL/OSL-DA-20, DTU Risø Campus, Roskilde, Denmark) equipped with a $^{90}Sr/^{90}Y$ beta source. Irradiation was performed at a dose rate of 0.086 Gy/s for 24 h prior to readout.

## 3. Results and Discussion

### *3.1. Reaction Mechanism*

The reaction mechanism for the growth of NCD films under Ar-rich conditions is based on models proposed for diamond CVD plasmas and for nanocrystalline diamond growth in $CH_4/Ar$ mixtures, with some modifications to account for the specific conditions of this work [18,26]. Although no $H_2$ is added to the gas mixture, the dissociation of $CH_4$ induced by electron impact and collisions with excited Ar species produces a family of $CH_x$ (x = 1–4) radicals and hydrogen atoms, which govern the gas-phase chemistry and the balance between $sp^3$ and $sp^2$ carbon [26].

$$Ar + e^- \rightarrow Ar^* + e^-, \quad (1)$$

where Ar* denotes excited (metastable) argon atoms generated by electron impact. These excited Ar species participate in methane activation. In the second stage, $CH_4$ dissociates, with the predominant formation of $CH_3$ radicals and H atoms through electron collisions and energy transfer from Ar* [26].

$$CH_4 + e^- \rightarrow CH_3 + H + e^-. \quad (2)$$

Hydrogen atoms drive a network of fast abstraction and addition reactions (H-shifting) that interconvert $CH_y$ species ($CH_4$, $CH_3$, $CH_2$, and CH). Consequently, their relative densities depend on the local H density and the gas thermal energy. In a simplified form, the following equilibrium can be represented as [26]:

$$CH_x + H \rightleftharpoons CH_{x-1} + H_2, \quad x = 1–4. \quad (3)$$

At a later stage, recombination of CH radicals leads to the formation of $C_2H_x$ species. A representative pathway is the formation of $C_2H_2$ from $CH_3$ radicals, followed by successive dehydrogenation steps to generate acetylene ($C_2H_2$) and, finally, $C_2$ [26,27]:

$$CH_3 + CH_3 + M \rightarrow C_2H_6 + M. \quad (4)$$

$$C_2H_6 \rightarrow C_2H_2 + 2H_2, \quad (5)$$

$$C_2H_2 \rightarrow C_2 + H_2. \quad (6)$$

where M is a neutral gas species (Ar or $CH_4$) acting as a third body in the recombination and providing the energy to stabilize $C_2H_6$ [26].

Under Ar-rich conditions and low hydrogen content, $C_2$ becomes an abundant gas-phase species, which has been specifically associated with nanocrystalline diamond growth in $CH_4/Ar$ plasmas [18,28].

### *3.2. Raman Spectroscopy*

Figure 2 shows the Raman spectra of the NCD films synthesized in this work. The two vertical dashed lines mark reference positions at 1332 $cm^{-1}$ and 1580 $cm^{-1}$, corresponding to the first-order Raman line of bulk diamond and to the G band of graphitic carbon in an ideal $sp^2$-bonded network, respectively. For the films grown at 300 °C and 400 °C, a pronounced band develops in the 1332–1335 $cm^{-1}$ region, which is assigned to the first-order diamond Raman line associated with $sp^3$-bonded carbon. In contrast, the broad

feature whose maximum appears around 1596 $cm^{-1}$ is attributed to the G band of $sp^2$-bonded carbon. The slight upshift of this maximum with respect to the 1580 $cm^{-1}$ reference is consistent with the behavior reported for disordered and nanostructured $sp^2$ carbon phases in diamond-like and nanocrystalline diamond films [29]. For the films grown at 300 °C and 400 °C, a pronounced band develops in the 1332–1335 $cm^{-1}$ region, which is assigned to the first-order diamond mode associated with $sp^3$-bonded carbon. Additionally, the broad band near 1600 $cm^{-1}$, known as the G band, reflects the presence of C-C bonds with $sp^2$ hybridization, commonly associated with grain boundary and graphitic structures in polycrystalline and nanocrystalline diamond films [29–31].

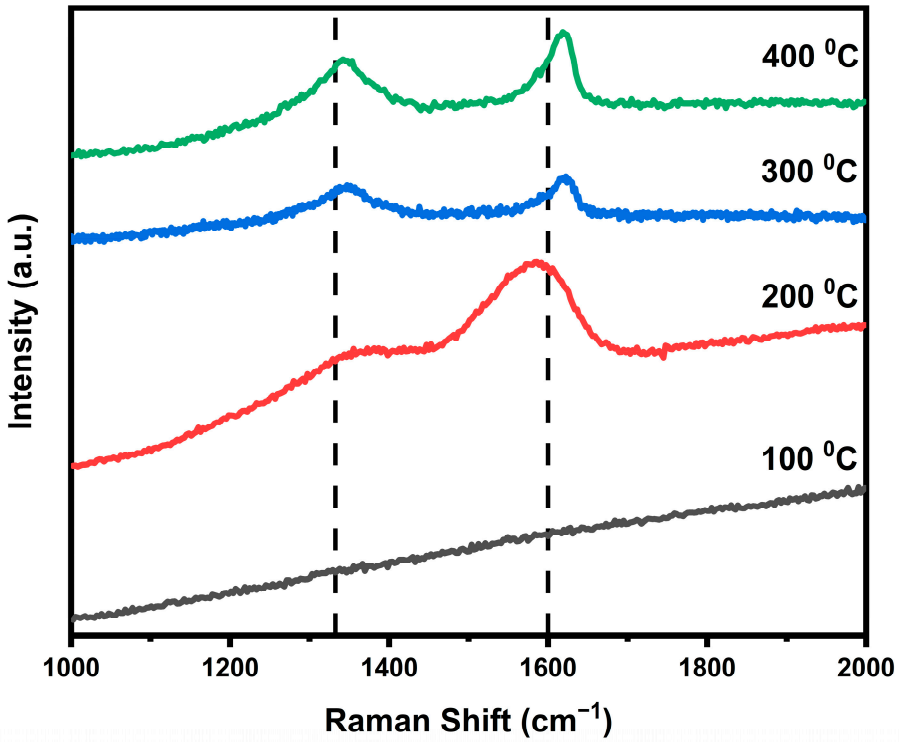


**Figure 2.** Raman spectra of NCD films grown at different substrate temperatures (100–400 °C). The vertical dashed lines mark the reference positions of the first-order Raman mode of bulk diamond (1332 $cm^{-1}$) and the G band of graphitic carbon (~1580 $cm^{-1}$).

Moreover, the structure evolution of NCD films as a function of temperature variations was observed in Raman spectra. At 100 °C, an increase in a featureless baseline is observed, suggesting the presence of amorphous carbon due to a deficiency in energy for crystalline diamond growth. As the temperature increases to 200 °C, a broad band appears in the spectra, suggesting structural organization within the carbon lattice. For the sample grown at 300 °C, the NCD films exhibit a diamond-related band at 1334 $cm^{-1}$, and a peak centered around 1622 $cm^{-1}$ becomes evident; the latter is associated with $sp^2$-bonded carbon and is commonly related to the graphitic content in the sample. These characteristic Raman modes imply the coexistence of diamond and graphite-like structures, commonly observed in diamond films synthesized at these temperatures, and reveal a transition in the carbon bond structure [32].

At 400 °C, the diamond-related band sharpens and shifts to 1335 $cm^{-1}$, while its intensity increases relative to the G band, indicating improved crystallinity of the NCD structure. According to the Raman results, increasing the synthesis temperature enhances the growth of C compounds into NCD structures, which is critical for applications requiring precise electronic and thermal properties. However, the presence of the G band peak

at 1598 $cm^{-1}$ shows that $sp^2$ bond vibrations persist and remain associated with grain boundaries in NCD films [33].

For a more detailed analysis, the Raman spectrum of the NCD film grown at 400 °C (Figure 3) was first corrected by subtracting a linear baseline and was subsequently fitted as a sum of Gaussian peak functions using a least-squares procedure. In Figure 3, the baseline-corrected experimental Raman spectrum is plotted as a black curve. The colored curves correspond to the individual Gaussian components of the fit; their sum reproduces the experimental spectrum.

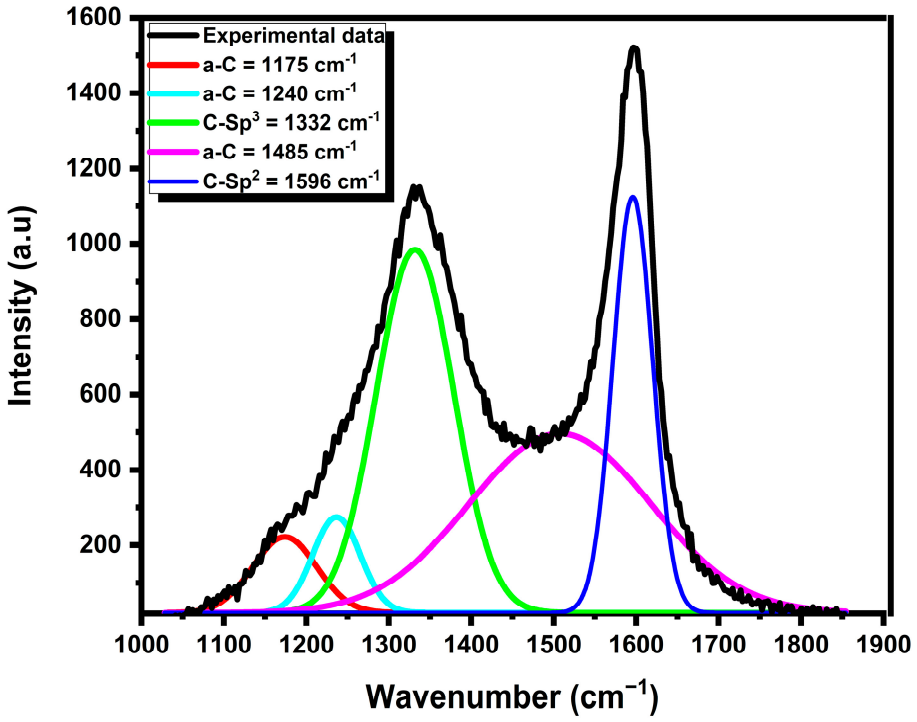


**Figure 3.** Curve-fitted Raman spectrum of a nanocrystalline diamond film synthesized by MPCVD with a substrate temperature of 400 °C, showing the D and G peaks along with amorphous carbon phases.

The band associated with diamond at 1331.81 $cm^{-1}$, corresponding to carbon in an $sp^3$ bonding configuration, confirms the presence of crystalline diamond-like phases in the sample. The G band, centered at 1596 $cm^{-1}$ and characteristic of $sp^2$ bonding, indicates the coexistence of graphitic phases at grain boundaries, a common feature in NCD films. Based on the integrated intensities (areas) of the diamond band at 1332 $cm^{-1}$ and the G band, approximately 63% of the combined Raman intensity of these two bands arises from $sp^3$-bonded carbon and 37% from $sp^2$-bonded carbon. The smaller peaks at 1175, 1240, and 1485 $cm^{-1}$ are attributed to amorphous or highly disordered carbon phases, reflecting structural disorder in specific regions of the NCD deposits. To clarify the origin of these additional Raman modes, Table 1 lists the main Raman peak positions, their possible chemical-bond assignments, and the corresponding references. The fitting parameters of the Raman components (peak position, FWHM, and integrated area) are summarized in Table S1 (Supporting Information) [34,35].

**Table 1.** Summary of Raman peak positions for diamond films.

| Peak Position ($cm^{-1}$) | Origin | Reference |
|---|---|---|
| 1596 | G peak of amorphous carbon | [34,35] |
| 1485 | Trans-polyacetylene-like polymeric adsorbate | [32,36,37] |
| 1350 | D peak from amorphous carbon | [38] |
| 1332 | Raman peak from diamond | [39] |
| 1240 | Scattering from the phonon at the L point from diamond | [36] |
| 1175 | Trans-polyacetylene | [32,36] |

Raman analysis demonstrated the progression from amorphous carbon to crystalline diamond with increasing synthesis temperature. These spectral transformations are reliable indicators of structural evolution in films, directly correlated with the synthesis parameters and the resulting film properties.

### *3.3. X-Ray Diffraction*

The crystallinity of the film grown at a substrate temperature of 400 °C was confirmed by X-ray diffraction (XRD) (see Figure 4). The pattern exhibits a sharp peak at $2\theta = 44.3°$, corresponding to the (111) plane of diamond, superimposed on a diffuse background. This result is consistent with reports by Auciello et al. on NCD films deposited by MPCVD, where the (111) orientation dominates due to the lower surface energy of this plane and the preferential incorporation of $CH_3$ radicals during growth [40,41]. The absence of additional peaks confirms that the predominant phase is diamond, and that the fraction of other residual phases is minimal, supporting the high $sp^3$ content inferred from the Raman analysis.

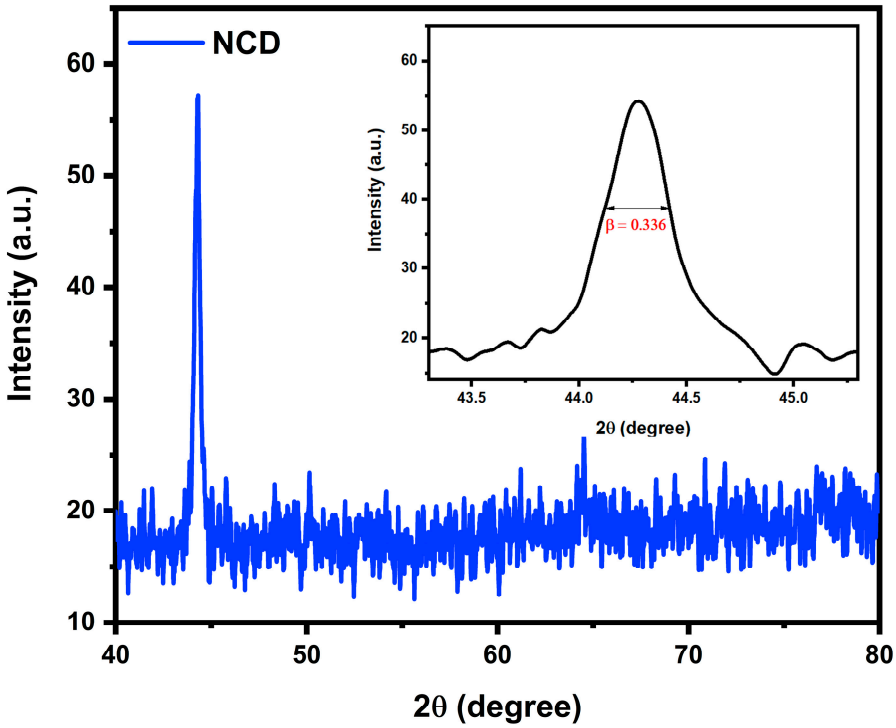


**Figure 4.** X-ray diffraction pattern (Cu Kα) of the NCD film. The dominant peak at $2\theta \approx 44.3°$ corresponds to the (111) reflection of cubic diamond. The inset shows a high-resolution view of this peak together with its Gaussian fit (red curve). From the fitted full width at half-maximum ($\beta = 0.336°$).

The crystallite size was estimated using the Scherrer equation [42]:

$$L = \frac{K\lambda}{\beta cos\theta}, \quad (7)$$

where $L$ is the average crystallite size, $K$ the shape factor (0.9 for quasi-spherical grains), $\lambda$ the wavelength of the Cu K$\alpha$ radiation (1.5406 Å), $\beta$ the full width at half-maximum (FWHM) of the (111) in radians, and $\theta$ the Bragg angle. Applying Equation (7) to the dominant peak at $2\theta = 44.3°$ yields $L = 26$ nm, consistent with the NCD nature of the films.

### *3.4. X-Ray Photoelectron Spectroscopy*

The XPS data were analyzed using a robust simultaneous fitting methodology, in which peak parameters were determined globally from the complete dataset rather than independently for each spectrum [43]. In this approach, a common set of binding energies was obtained self-consistently and subsequently applied to all samples.

The resulting binding energies for the C 1s components were 284.4 ± 0.2 eV ($sp^2$), 285.4 ± 0.2 eV ($sp^3$), 286.4 ± 0.3 eV (C–OH), and 287.5 ± 0.2 eV (C=O).

The peak shapes were modeled using Voigt profiles. The Lorentzian component was fixed at 0.35 eV for all peaks and all samples, while the Gaussian width was correlated with all peaks within each individual spectrum but allowed to vary between samples. This strategy ensures internal consistency of peak shapes within a given spectrum while still allowing for temperature-dependent changes in spectral broadening. Under these constraints, the peak intensities were the primary parameters varying across the dataset.

Figure 5 shows the XPS spectra obtained from the NCD films synthesized in this work. The spectra were fitted using the O 1s peak of C=O and the C 1s peak of Carbon $sp^2$ (green line), reported to have a binding energy of 531 ± 0.6 eV and 284.4 ± 0.2 eV, respectively [44,45]. The C $sp^3$ peak located at 285.4 ± 0.2 eV (purple line) is associated with diamond structures. Additionally, other carbon species, such as hydrocarbons (C-OH, yellow line at 286.4 eV) and carboxyl groups (C=O, cyan line at 287.5 eV), were detected by XPS analysis [44,46]. These peaks, attributed to C-OH and C=O, are associated with the amorphous carbon present in the film.

The XPS spectra show binding-energy peaks attributed to different types of carbon bonds, such as $sp^2$ and $sp^3$ hybridizations, which correlate with the previously discussed Raman spectroscopy data. The NCD films grown at 100 °C and 200 °C, presented in Figures 5a and 5b, respectively, exhibit a significant presence of $sp^2$-hybridized bonds, indicating graphitic or disordered carbon structures. However, as the substrate temperature rises to 300 °C and 400 °C, as shown in Figures 5c and 5d, respectively, a significant increase in the intensity of $sp^3$ hybridized bonds was observed, indicating the formation of more crystalline diamond structures. In addition, the XPS peaks corresponding to oxygen-containing functional groups, such as C=O and C-OH, become more evident as temperature increases. The latter indicates that oxidative processes occur at the surface of NCD films due to interactions with oxygen during or after deposition, introducing surface functionalities that can modify the NCD films' electronic properties [47]

The quantitative data in Table 2 complement the XPS spectra, providing a clear representation of the change in bond states with temperature. At 100 °C, the high $sp^2$ hybridization content (85.62%) suggests a predominantly graphitic structure. However, as the temperature increased, a progressive decrease in $sp^2$ hybridized carbon to 61.30% at 400 °C was observed, accompanied by a corresponding increase in $sp^3$ hybridization from 14.38% to 38.70%. This progression supports the transition from amorphous and graphitic carbon structures to an NCD structure with a higher proportion of $sp^3$ hybridized bonds.

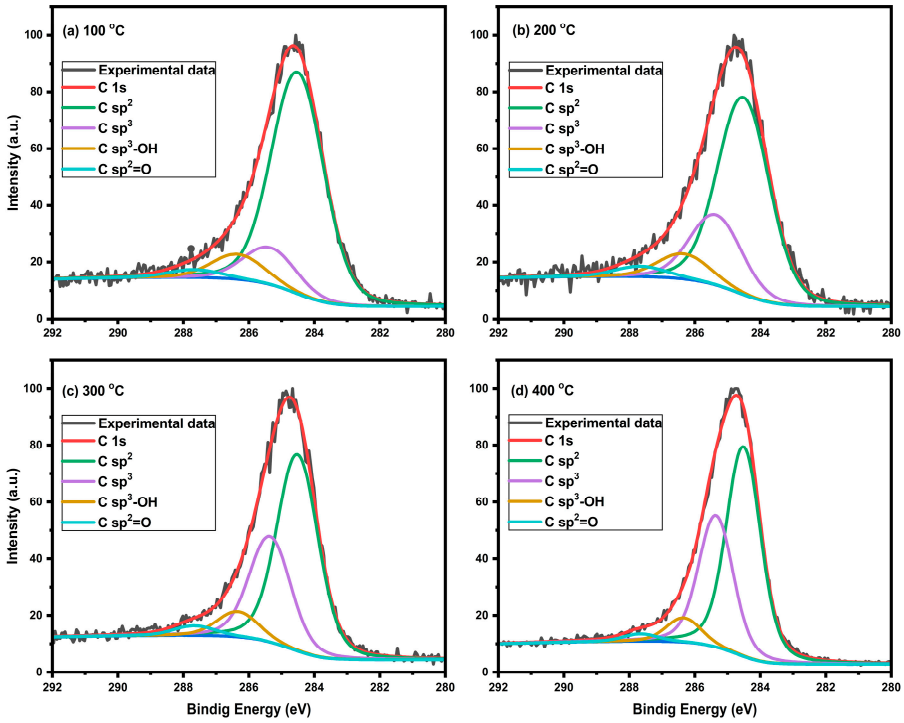


**Figure 5.** XPS spectra of NCD films at substrate temperatures of (**a**) 100 °C, (**b**) 200 °C, (**c**) 300 °C, and (**d**) 400 °C, showing the distribution of $sp^2$, $sp^3$, and oxygen-containing carbon species. The grey curve corresponds to the experimental XPS spectrum (experimental data), while the colored curves represent the fitted components.

**Table 2.** Relative $sp^2$ and $sp^3$ carbon contributions obtained from C 1s XPS peak fitting, together with the Gaussian widths used in the Voigt profiles for each substrate temperature. The Lorentzian width was fixed at 0.35 eV for all peaks, and a common set of binding energies was applied to all samples.

| Ts (°C) | % Area C $sp^2$ | % Area C $sp^3$ | Gaussian Widths |
|---|---|---|---|
| 100 | 85.62 | 14.38 | 1.71 |
| 200 | 73.60 | 26.40 | 1.73 |
| 300 | 64.85 | 35.15 | 1.27 |
| 400 | 61.30 | 38.70 | 1.04 |

To ensure a consistent comparison across temperatures, all XPS spectra were fitted using Voigt profiles with a fixed Lorentzian width of 0.35 eV. The Gaussian widths were correlated for all peaks within each spectrum, and a common set of binding energies was applied to every sample. These constraints ensure that the peak positions and widths remain the same throughout the temperature series, so any changes observed in the C $sp^2$ and C $sp^3$ components arise solely from variations in their integrated intensities. The increase in $sp^3$ intensity at higher temperatures, therefore, reflects a genuine modification of the bonding environment in the films. Higher substrate temperatures enhance hydrogen-assisted etching of graphitic carbon, reduce the amount of $sp^2$-rich grain boundary material, and promote diamond grain growth. These mechanisms reduce the relative surface abundance of $sp^2$ carbon while increasing the contribution of $sp^3$ bonding, consistent with the trends observed in Raman spectroscopy.

Raman and XPS results show structural evolution in NCD films as the substrate temperature increases. The rise in the proportion of $sp^3$ bonds relative to $sp^2$ is consistent across both techniques, indicating a transition from an amorphous and graphitic structure to a crystalline diamond structure.

To clarify the effect of substrate temperature on the growth evolution of NCD films obtained by MPCVD in this work, we summarize here the main trends observed in the Raman and XPS analyses. At 100 °C and 200 °C, the deposited carbon samples exhibit a higher degree of disorder, reflecting a larger graphitic contribution in the films. However, at 300 °C and 400 °C, an increase in crystallinity was observed, favoring the diamond phase over the graphitic phase, as evidenced by Raman and XPS spectra showing increased $sp^3$ bonding. This indicates a structural transition towards the production of higher-quality material, consistent with XPS analysis, which reveals an increase in the proportion of NCD in the samples at higher temperatures.

### *3.5. Scanning Electron Microscopy (SEM)*

Figure 6 shows the top-view and cross-section SEM images of the NCD films synthesized at 400 °C. Figure 6a exhibits agglomerated grains with a particle size distribution of approximately 45 nm. Furthermore, a spheroidal trending morphology with sharp edges and a homogeneous surface, as expected for NCD films, was observed [12]. In Figure 6b, an NCD film cross-section is shown, with a thickness of 270 nm and high homogeneity in the NCD layer thickness along the sample.

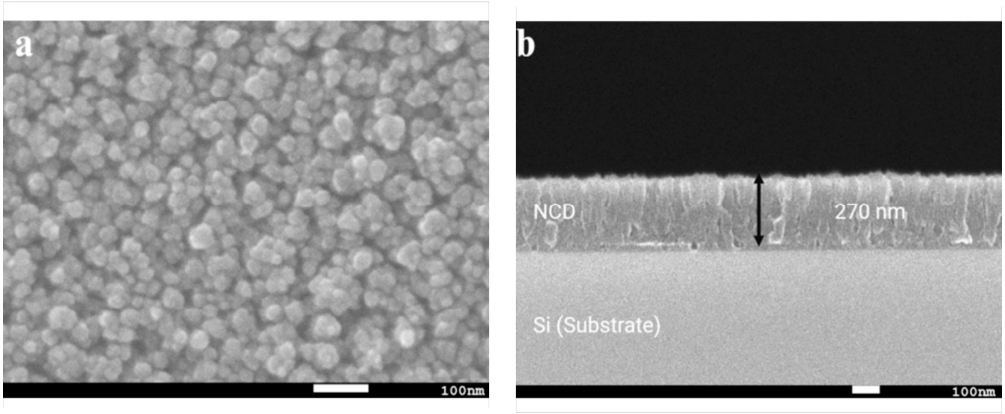


**Figure 6.** SEM images of NCD films synthesized at 400 °C: (**a**) plan view showing agglomerated grains with an approximate size of 45 nm and (**b**) cross-section view displaying a uniform thickness of 270 nm.

### *3.6. Thermoluminescence (TL)*

The thermoluminescence (TL) curve of the nanocrystalline diamond (NCD) film grown at 400 °C, shown in Figure 7 exhibits two brightness maxima (Tm) located at 157 °C and 270 °C, corresponding to different energy traps within the material. The peak at 157 °C can be associated with impurities, identified as substitutional atoms related to defects, which generate low-energy traps due to their weak interaction with the crystal lattice [48,49]. Although the synthesis process employed only methane and argon in the gas mixture, contamination is common in MPCVD systems and can introduce impurities in concentrations sufficient to form substitutional defects [49].

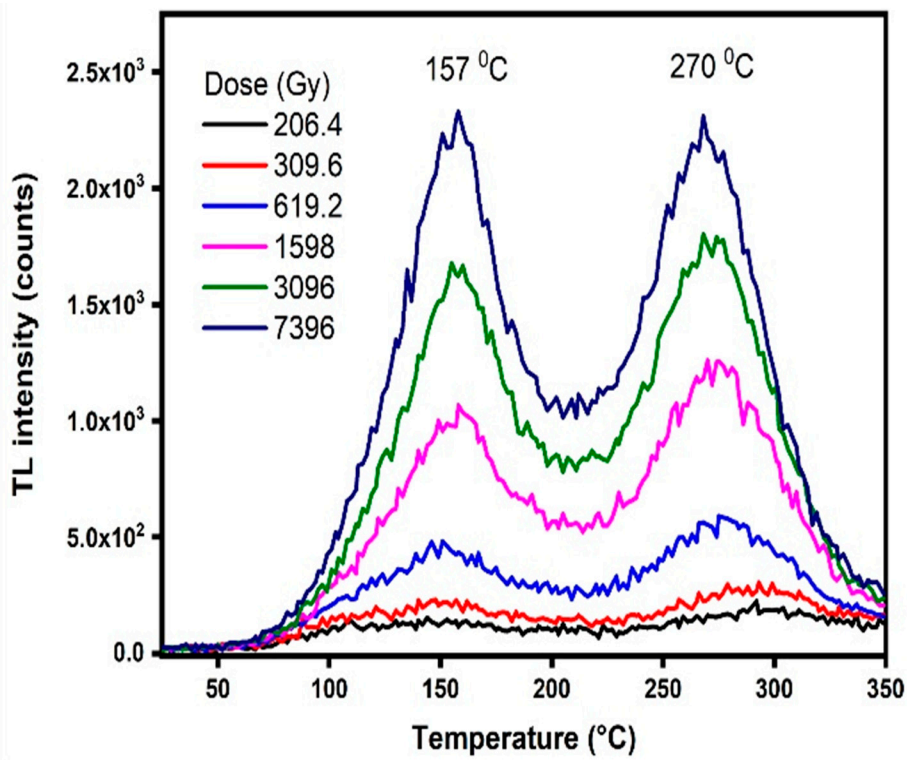


**Figure 7.** Thermoluminescence (TL) curve of nanocrystalline diamond (NCD) film synthesized at a substrate temperature of 400 °C, showing TL maxima at 157 °C and 270 °C under varying radiation doses.

On the other hand, the peak at 270 °C is associated with $sp^3$ carbon structures, as confirmed by XPS and Raman analyses, indicating the crystalline bonds characteristic of diamond [50,51]. This peak is interpreted as the release of energy from traps associated with vacancies or interstitial sites stabilized by the tetrahedral configuration of $sp^3$ bonds, which also implies higher thermal stability for these traps [48,50]. This behavior is particularly relevant for dosimetry applications, as the stability and high-dose response of these traps enable precise measurements and reliable recording of radiation exposure. Thus, the NCD films synthesized using this method demonstrate potential for dosimetry applications.

## 4. Conclusions

We demonstrated a hydrogen-free, seedless route to grow NCD by MPCVD ($CH_4$/Ar) at 100–400 °C on p-type Si(111). XRD of the 400 °C sample shows a broad (111) reflection at $2\theta \approx 44.4°$, from which a crystallite size of ~23 nm was estimated via the Scherrer equation, consistent with nanocrystalline $sp^3$ domains. Raman and XPS evidence an increase in the $sp^3$ fraction between 300 and 400 °C, while SEM reveals continuous, uniform films. TL glow curves exhibit peaks at ~157 °C and ~270 °C, associated with electron traps compatible with a dosimetric response. Overall, these results confirm the feasibility of low-thermal-load NCD growth without $H_2$ or seeding and support its potential for electronic and dosimetric applications. As a next step, a broader TL study is proposed to consolidate performance validation.

**Supplementary Materials:** The following supporting information can be downloaded at: https://www.mdpi.com/article/10.3390/cryst16010010/s1, Table S1: Fitting parameters of the Raman spectrum of the NCD film grown at 400 °C (Figure 3). Gaussian peak position, full width at half maximum (FWHM) and integrated area for each component. Table S2: Integrated TL intensities of the low- and high-temperature peaks as a function of absorbed dose, and corresponding intensity ratio $I_{High}/I_{Low}$.

**Author Contributions:** Conceptualization, L.M.-Z. and R.G.-G.; methodology, investigation, data curation, visualization, and writing—original draft, L.M.-Z.; validation and formal analysis, all authors; resources, M.M.-G. (Miguel Martínez-Gil) and C.A.P.-R.; writing—review and editing, all authors; supervision, D.B.-M., A.R.-C., C.A.P.-R. and R.G.-G.; project administration and funding acquisition, R.F.-O., M.M.-G. (Mathias Martínez-Gil), D.B.-M., A.R.-C., C.A.P.-R. and R.G.-G. All authors have read and agreed to the published version of the manuscript.

**Funding:** This research received no external funding.

**Data Availability Statement:** The data presented in this study are available on reasonable request from the corresponding author. The data are not publicly available due to institutional policy and data management constraints.

**Acknowledgments:** The authors thank the Secretaría de Ciencia, Humanidades, Tecnología e Innovación (SECIHTI) for financial support., National Solar Energy Association (ANES), NanoFAB Laboratory (272894), National Laboratory LaNNAFab (294452) and the University of Sonora for its facilities and the material provided to accomplish this work. We also thank Roberto Mora Monroy, Roberto Carlos Carrillo Torres, Monica Alessandra Acosta Elias, Francisco Brown Bojórquez and, in general, to the Department of Research in Polymers and Materials. During the preparation of this manuscript, the authors used ChatGPT (OpenAI, San Francisco, CA, USA; https://chat.openai.com accessed on 15 November 2025; model: GPT-5.2) and Grammarly (Grammarly Inc. San Francisco, CA, USA; https://www.grammarly.com accessed on 21 November 2025) exclusively for grammar and language corrections. The authors reviewed and edited all generated output and take full responsibility for the content of this publication.

**Conflicts of Interest:** The authors declare no competing financial or non-financial interest. The funding agencies had no role in the design of the study; in the collection, analyses, or interpretation of data; in the writing of the manuscript; or in the decision to publish the results.

## Abbreviations

The following abbreviations are used in this manuscript:

| | |
|---|---|
| NCD | Nanocrystalline diamond |
| CVD | Chemical Vapor Deposition |
| HFCVD | Hot-filament chemical vapor deposition |
| MPCVD | Microwave plasma chemical vapor deposition |
| XRD | X-ray diffraction |
| GIXRD | Grazing-incidence X-ray diffraction |
| XPS | X-ray photoelectron spectroscopy |
| SEM | Scanning electron microscopy |
| TL | Thermoluminescence |

## References

1. Bull, S.J.; Matthews, A. Diamond for Wear and Corrosion Applications. *Diam. Relat. Mater.* **1992**, *1*, 1049–1064. [CrossRef]
2. Krainsky, I.L.; Asnin, V.M. Negative Electron Affinity Mechanism for Diamond Surfaces. *Appl. Phys. Lett.* **1998**, *72*, 2574–2576. [CrossRef]
3. Marotta, E.; Bakhru, N.; Grill, A.; Patel, V.; Meyerson, B. Diamond-like Carbon as an Electrical Insulator of Copper Devices for Chip Cooling. *Thin Solid Films* **1991**, *206*, 188–191. [CrossRef]
4. Morelli, D.T.; Beetz, C.P.; Perry, T.A. Thermal Conductivity of Synthetic Diamond Films. *J. Appl. Phys.* **1988**, *64*, 3063–3066. [CrossRef]
5. Narayan, J.; Fan, W.D.; Narayan, R.J.; Tiwari, P.; Stadelmaier, H.H. Diamond, Diamond-like and Titanium Nitride Biocompatible Coatings for Human Body Parts. *Mater. Sci. Eng. B* **1994**, *25*, 5–10. [CrossRef]
6. Nistor, P.A.; May, P.W. Diamond Thin Films: Giving Biomedical Applications a New Shine. *J. R. Soc. Interface* **2017**, *14*, 20170382. [CrossRef]
7. Tirado, P.; Alcantar-Peña, J.J.; De Obaldia, E.; Kudriavtsev, Y.; García, R.; Auciello, O. Boron Doping of Ultrananocrystalline Diamond Films by Thermal Diffusion Process. *MRS Commun.* **2018**, *8*, 1111–1118. [CrossRef]

8. Matsumoto, S. Chemical Vapour Deposition of Diamond in RF Glow Discharge. *J. Mater. Sci. Lett.* **1985**, *4*, 600–602. [CrossRef]
9. Ohtake, N.; Yoshikawa, M. Diamond Film Preparation by Arc Discharge Plasma Jet Chemical Vapor Deposition in the Methane Atmosphere. *J. Electrochem. Soc.* **1990**, *137*, 717–722. [CrossRef]
10. Suzuki, K.; Sawabe, A.; Yasuda, H.; Inuzuka, T. Growth of Diamond Thin Films by Dc Plasma Chemical Vapor Deposition. *Appl. Phys. Lett.* **1987**, *50*, 728–729. [CrossRef]
11. Mokuno, Y.; Chayahara, A.; Yamada, H. Synthesis of Large Single Crystal Diamond Plates by High Rate Homoepitaxial Growth Using Microwave Plasma CVD and Lift-off Process. *Diam. Relat. Mater.* **2008**, *17*, 415–418. [CrossRef]
12. Fuentes-Fernandez, E.M.A.; Alcantar-Peña, J.J.; Lee, G.; Boulom, A.; Phan, H.; Smith, B.; Nguyen, T.; Sahoo, S.; Ruiz-Zepeda, F.; Arellano-Jimenez, M.J.; et al. Synthesis and Characterization of Microcrystalline Diamond to Ultrananocrystalline Diamond Films via Hot Filament Chemical Vapor Deposition for Scaling to Large Area Applications. *Thin Solid Films* **2016**, *603*, 62–68. [CrossRef]
13. Weng, J.; Liu, F.; Wang, Z.T.; Guo, N.F.; Fan, F.Y.; Yang, Z.; Wang, J.B.; Wang, H.; Xiong, L.W.; Zhao, H.Y.; et al. Investigation on the Preparation of Large Area Diamond Films with 150–200 Mm in Diameter Using 915 MHz MPCVD System. *Vacuum* **2023**, *217*, 112543. [CrossRef]
14. Alcantar-Peña, J.J.; de Obaldia, E.; Montes-Gutierrez, J.; Kang, K.; Arellano-Jimenez, M.J.; Ortega Aguilar, J.E.; Suchy, G.P.; Berman-Mendoza, D.; Garcia, R.; Yacaman, M.J.; et al. Fundamentals towards Large Area Synthesis of Multifunctional Ultrananocrystalline Diamond Films via Large Area Hot Filament Chemical Vapor Deposition Bias Enhanced Nucleation/Bias Enhanced Growth for Fabrication of Broad Range of Multifunctional Devices. *Diam. Relat. Mater.* **2017**, *78*, 1–11. [CrossRef]
15. Ali, M.; Ürgen, M.; Kawashima, A. High Purity Diamond Films Synthesised by Chemical Vapour Deposition. *Surf. Eng.* **2012**, *28*, 791–795. [CrossRef]
16. Das, D.; Singh, R.N. A Review of Nucleation, Growth and Low Temperature Synthesis of Diamond Thin Films. *Int. Mater. Rev.* **2007**, *52*, 29–64. [CrossRef]
17. Yang, L.; Jiang, C.; Guo, S.; Zhang, L.; Gao, J.; Peng, J.; Hu, T.; Wang, L. Novel Diamond Films Synthesis Strategy: Methanol and Argon Atmosphere by Microwave Plasma CVD Method Without Hydrogen. *Nanoscale Res. Lett.* **2016**, *11*, 4–9. [CrossRef]
18. Zhou, D.; McCauley, T.G.; Qin, L.C.; Krauss, A.R.; Gruen, D.M. Synthesis of Nanocrystalline Diamond Thin Films from an Ar-CH4 Microwave Plasma. *J. Appl. Phys.* **1998**, *83*, 540–543. [CrossRef]
19. Sternberg, M.; Zapol, P.; Curtiss, L.A. Carbon Dimers on the Diamond (100) Surface: Growth and Nucleation. *Phys. Rev. B—Condens. Matter Mater. Phys.* **2003**, *68*, 205330. [CrossRef]
20. Xiao, X.; Birrell, J.; Gerbi, J.E.; Auciello, O.; Carlisle, J.A. Low Temperature Growth of Ultrananocrystalline Diamond. *J. Appl. Phys.* **2004**, *96*, 2232–2239. [CrossRef]
21. Alcantar-Peña, J.J.; Montes, J.; Arellano-Jimenez, M.J.; Aguilar, J.E.O.; Berman-Mendoza, D.; García, R.; Yacaman, M.J.; Auciello, O. Low Temperature Hot Filament Chemical Vapor Deposition of Ultrananocrystalline Diamond Films with Tunable Sheet Resistance for Electronic Power Devices. *Diam. Relat. Mater.* **2016**, *69*, 207–213. [CrossRef]
22. Zeng, H.; Arumugam, P.U.; Siddiqui, S.; Carlisle, J.A. Low Temperature Boron Doped Diamond. *Appl. Phys. Lett.* **2013**, *102*, 223108. [CrossRef]
23. McCauley, T.G.; Gruen, D.M.; Krauss, A.R. Temperature Dependence of the Growth Rate for Nanocrystalline Diamond Films Deposited from an Ar/CH4 Microwave Plasma. *Appl. Phys. Lett.* **1998**, *73*, 1646–1648. [CrossRef]
24. Mandal, S. Nucleation of Diamond Films on Heterogeneous Substrates: A Review. *RSC Adv.* **2021**, *11*, 10159–10182. [CrossRef]
25. Schmitz, J. Low Temperature Thin Films for Next-Generation Microelectronics (Invited). *Surf. Coatings Technol.* **2018**, *343*, 83–88. [CrossRef]
26. Butler, J.E.; Mankelevich, Y.A.; Cheesman, A.; Ma, J.; Ashfold, M.N.R. Understanding the Chemical Vapor Deposition of Diamond: Recent Progress. *J. Phys. Condens. Matter* **2009**, *21*, 364201. [CrossRef]
27. Kulisch, W.; Popov, C. On the Growth Mechanisms of Nanocrystalline Diamond Films. *Phys. Status Solidi Appl. Mater. Sci.* **2006**, *203*, 203–219. [CrossRef]
28. Auciello, O. Review of Materials Science and Technological Applications of a Unique Transformational Multifunctional Ultrananocrystalline Diamond (UNCD) Coating. *J. Biomed. Res. Environ. Sci.* **2024**, *5*, 1291–1304. [CrossRef]
29. Ferrari, A.C.; Robertson, J. Resonant Raman Spectroscopy of Disordered, Amorphous, and Diamondlike Carbon. *Phys. Rev. B—Condens. Matter Mater. Phys.* **2001**, *64*, 075414. [CrossRef]
30. Dychalska, A.; Fabisiak, K.; Paprocki, K.; Makowiecki, J.; Iskaliyeva, A.; Szybowicz, M. A Raman Spectroscopy Study of the Effect of Thermal Treatment on Structural and Photoluminescence Properties of CVD Diamond Films. *Mater. Des.* **2016**, *112*, 320–327. [CrossRef]
31. Williams, O.A.; Nesládek, M. Growth and Properties of Nanocrystalline Diamond Films. *Phys. Status Solidi Appl. Mater. Sci.* **2006**, *203*, 3375–3386. [CrossRef]
32. Ferrari, A.C.; Robertson, J. Origin of the 1150 − $Cm^{-1}$ Raman Mode in Nanocrystalline Diamond. *Phys. Rev. B—Condens. Matter Mater. Phys.* **2001**, *63*, 121405. [CrossRef]

33. Shroder, R.E.; Nemanich, R.J.; Glass, J.T. Analysis of the Composite Structures in Diamond Thin Films by Raman Spectroscopy. *Phys. Rev. B* **1990**, *41*, 3738–3745. [CrossRef]
34. Ramamurti, R.; Shanov, V.; Singh, R.N.; Mamedov, S.; Boolchand, P. Raman Spectroscopy Study of the Influence of Processing Conditions on the Structure of Polycrystalline Diamond Films. *J. Vac. Sci. Technol. A Vacuum Surfaces Film.* **2006**, *24*, 179–189. [CrossRef]
35. Ramos, S.C.; Azevedo, A.F.; Baldan, M.R.; Ferreira, N.G. Effect of Methane Addition on Ultrananocrystalline Diamond Formation: Morphology Changes and Induced Stress. *J. Vac. Sci. Technol. A Vacuum Surfaces Film.* **2010**, *28*, 27–32. [CrossRef]
36. López-Ríos, T.; Sandré, É.; Leclercq, S.; Sauvain, É. Polyacetylene in Diamond Films Evidenced by Surface Enhanced Raman Scattering. *Phys. Rev. Lett.* **1996**, *76*, 4935–4938. [CrossRef]
37. Muranaka, Y.; Yamashita, H.; Miyadera, H. Characterization of Diamond Films Synthesized in the Microwave Plasmas of $CO/H_2$ and $CO/O_2/H_2$ Systems at Low Temperatures (403–1023 K). *J. Appl. Phys.* **1991**, *69*, 8145–8153. [CrossRef]
38. Knight, D.S.; Weimer, R.; Pilione, L.; White, W.B. Surface-Enhanced Raman Spectroscopy of Chemical Vapor Deposited Diamond Films. *Appl. Phys. Lett.* **1990**, *56*, 1320–1322. [CrossRef]
39. Solin, S.A.; Ramdas, A.K. Raman Spectrum of Diamond. *Phys. Rev* **1969**, *B1*, 1687. [CrossRef]
40. Auciello, O.; Sumant, A.V. Status Review of the Science and Technology of Ultrananocrystalline Diamond ($UNCD^{TM}$) Films and Application to Multifunctional Devices. *Diam. Relat. Mater.* **2010**, *19*, 699–718. [CrossRef]
41. Chu, Y.C.; Tzeng, Y.; Auciello, O. Microwave Plasma Enhanced Chemical Vapor Deposition of Nanocrystalline Diamond Films by Bias-Enhanced Nucleation and Bias-Enhanced Growth. *J. Appl. Phys.* **2014**, *115*, 024308. [CrossRef]
42. Langford, J.I.; Wilson, A.J.C. Scherrer after Sixty Years: A Survey and Some New Results in the Determination of Crystallite Size BY. *J. Appl. Crystallogr.* **1978**, *11*, 102–113. [CrossRef]
43. Muñoz-Flores, J.; Herrera-Gomez, A. Resolving Overlapping Peaks in ARXPS Data: The Effect of Noise and Fitting Method. *J. Electron Spectros. Relat. Phenom.* **2012**, *184*, 533–541. [CrossRef]
44. Becerra-Paniagua, D.K.; Cabrera-German, D.; Díaz-Cruz, E.B.; Montiel-González, Z.; Sotelo-Lerma, M.; Hu, H. Dispersion Degree and Sheet Spacing Control of Graphene Products via Oxygen Functionalities and Its Effect on Electrical Conductivities of P3HT-Graphene Composite Coatings. *J. Mater. Sci. Mater. Electron.* **2020**, *31*, 19623–19637. [CrossRef]
45. Stobinski, L.; Lesiak, B.; Malolepszy, A.; Mazurkiewicz, M.; Mierzwa, B.; Zemek, J.; Jiricek, P.; Bieloshapka, I. Graphene Oxide and Reduced Graphene Oxide Studied by the XRD, TEM and Electron Spectroscopy Methods. *J. Electron Spectros. Relat. Phenomena* **2014**, *195*, 145–154. [CrossRef]
46. Sheng, H.; Xiong, W.; Zheng, S.; Chen, C.; He, S.; Cheng, Q. Evaluation of the $Sp^3/Sp^2$ Ratio of DLC Films by RF-PECVD and Its Quantitative Relationship with Optical Band Gap. *Carbon Lett.* **2021**, *31*, 929–939. [CrossRef]
47. Torrengo, S.; Canteri, R.; Dell'Anna, R.; Minati, L.; Pasquarelli, A.; Speranza, G. XPS and ToF-SIMS Investigation of Nanocrystalline Diamond Oxidized Surfaces. *Appl. Surf. Sci.* **2013**, *276*, 101–111. [CrossRef]
48. Collins, A.T. Optical Centres Produced in Diamond by Radiation Damage. *New Diam. Front. Carbon Technol.* **2007**, *17*, 47–61.
49. Sharda, T.; Sikder, A.K.; Misra, D.S.; Collins, A.T.; Bhargava, S.; Bist, H.D.; Veluchamy, P.; Minoura, H.; Kabiraj, D.; Awasthi, D.K.; et al. Studies of Defects and Impurities in Diamond Thin Films. *Diam. Relat. Mater.* **1998**, *7*, 250–254. [CrossRef]
50. Apátiga, L.M.; Golzarri, J.I.; Mumford, J.; Alba, F.; Castaño, V.M. Thermoluminescence of Diamond Films Induced by Beta Irradiation. *Radiat. Phys. Chem.* **1999**, *54*, 223–228. [CrossRef]
51. Montes-Gutiérrez, J.A.; Alcantar-Peña, J.J.; de Obaldia, E.; Zúñiga-Rivera, N.J.; Chernov, V.; Meléndrez-Amavizca, R.; Barboza-Flores, M.; Garcia-Gutierrez, R.; Auciello, O. Afterglow, Thermoluminescence and Optically Stimulated Luminescence Characterization of Micro-, Nano- and Ultrananocrystalline Diamond Films Grown on Silicon by HFCVD. *Diam. Relat. Mater.* **2018**, *85*, 117–124. [CrossRef]


**Disclaimer/Publisher's Note:** The statements, opinions and data contained in all publications are solely those of the individual author(s) and contributor(s) and not of MDPI and/or the editor(s). MDPI and/or the editor(s) disclaim responsibility for any injury to people or property resulting from any ideas, methods, instructions or products referred to in the content.